PHOTONICS Research

Dual-mode distributed feedback quantum cascade laser based on stacked 3D monolithic integration for on-chip multi-channel gas sensing

Xiyu Lu,[1,2] Yanjiao Guan,[1,2] Pengchang Yang,[1,2] Shan Niu,[1,2] Yu Ma,[1,2] Lijun Wang,[1,2] Ning Zhuo,[1,2] Jinchuan Zhang,[1,2] Shenqiang Zhai,[1,2] Fengmin Cheng,[1,2] Shuman Liu,[1,2] Fengqi Liu,[1,2] and Junqi Liu[1,2,*]

[1]Key Laboratory of Semiconductor Materials Science, Institute of Semiconductors, Chinese Academy of Sciences, Beijing Key Laboratory of Low Dimensional Semiconductor Materials and Devices, Beijing 100083, China
[2]Center of Materials Science and Optoelectronics Engineering, University of Chinese Academy of Sciences, Beijing 100049, China
*Corresponding author: jqliu@semi.ac.cn

Received 12 July 2023; revised 23 September 2023; accepted 7 October 2023; posted 11 October 2023 (Doc. ID 500047); published 24 November 2023

To facilitate the development of on-chip integrated mid-infrared multi-channel gas sensing systems, we propose a high-power dual-mode (7.01 and 7.5 μm) distributed feedback quantum cascade laser based on stacked 3D monolithic integration. Longitudinal mode control is achieved by preparing longitudinal nested bi-periodic compound one-dimensional Bragg gratings along the direction of the cavity length in the confinement layer. Additionally, transverse coherent coupling ridges perpendicular to the cavity length direction are fabricated in the upper waveguide layer to promote the fundamental transverse mode output when all ridges are in phase. Stable dual-wavelength simultaneous emission with a side-mode suppression ratio of more than 20 dB was achieved by holographic exposure and wet etching. The entire spectral tuning range covers nearly 100 nm through joint tuning of the injection current and heat-sink temperature. High peak power and beam quality are guaranteed by the parallel coherent integration of seven-element ridge arrays. The device operates in a fundamental supermode with a single-lobed far-field pattern, and its peak output power reaches 3.36 W in pulsed mode at 20°C. This dual-mode laser chip has the potential for *in-situ* on-chip simultaneous detection of CH_4 and C_2H_6 gases in leak monitoring.

https://doi.org/10.1364/PRJ.500047

1. INTRODUCTION

In recent years, extensive research has been conducted on quantum cascade lasers (QCLs) for operation in the mid-infrared spectral region with dense gas molecular absorption lines [1–4]. Trace gases within the QCL spectral coverage, such as CH_4, C_2H_6, N_2O, and SO_2, have gained significant attention for environmental monitoring [5], medical analysis [6], and *in-situ* atmospheric detection of the Earth and other planets [7,8]. Taking the application in the fields of oil and natural gas as an example, detecting the intensity ratio of CH_4 and C_2H_6 is necessary to diagnose natural gas pipeline leakage by determining whether the measured leaking gas is from natural gas, underground biogas, or other combustible gases [9]. In these cases, multiple gases must often be detected simultaneously [7,10]. At present, to avoid carrying multiple lasers [11,12], the simultaneous detection of multiple gases mainly relies on wavelength scanning (laser array) [13] absorption spectroscopy. Furthermore, remote detection and other applications also require high output power and a low divergence angle. Recently, Karnik *et al.* reported on the applicability of arrayed waveguide gratings (AWGs) in mid-infrared InGaAs/InP material platforms for effective wavelength beam combinations [14], which demonstrates the feasibility of applying the inverse process for wavelength division to implement multi-channel gas sensing through a passive waveguide. By this way, to achieve high-precision on-chip spectral detection of multiple gases, the input terminal must have dual- or multi-mode operation with a high side-mode suppression ratio (SMSR) at the target absorption lines, in addition to high beam quality and high output power.

These goals fundamentally require effective regulation of both the longitudinal and transverse modes of QCLs while increasing their output power. To achieve frequency-specific longitudinal mode outputs, distribution feedback (DFB) gratings are introduced into the upper confinement layer or surface [15,16]. Optimized multi-core materials, sampling gratings, and compound grating preparation are adopted to realize multiple frequency-specific longitudinal mode outputs with a high SMSR in a single laser [17–20]. Note that most of the above approaches with DFB gratings degrade the output power because of the influence of grating coupling strength [2,21,22]. Larger output power can be extracted by increasing the gain volume [23,24]. Simply increasing the ridge width, however, in turn generates higher-order transverse mode and deteriorates the beam quality in the form of the multi-lobe far field [25]. Photonic-crystal structures and coherent control via radio-frequency injection have been investigated in recent years for suppressing higher-order transverse modes [26,27]. The phase locking of the optical field between integrated ridge array elements is another valuable way to balance high power and lateral mode control [28,29]. Nevertheless, achieving the aforementioned requirements in a single device remains an engineering challenge owing to the presence of trade-offs and competing optimization goals.

In this work, we demonstrate a tunable dual-wavelength (λ_1 of ~7.5 μm and λ_2 of ~7.01 μm) QCL with high beam quality and high output power, which is based on a three-dimensional (3D) stacked monolithic integration solution. Along the direction of the cavity length, bi-periodic composite buried DFB gratings achieve dual frequency-specific longitudinal mode selection. The ridge array is arranged along the direction of ridge width, and coherent coupling forms a transverse fundamental mode while increasing the effective ridge width to improve output power. The structures are stacked on one ridge along the growth direction and fabricated in the upper confinement layer and the upper waveguide layer. The laser based on this technology maintains a stable dual longitudinal mode operation during temperature tuning from −4°C to 60°C, and the temperature tuning coefficients for λ_1 and λ_2 are −0.116 and −0.121 $cm^{-1}\,K^{-1}$, respectively. By combining current and temperature tuning, the device can cover a spectral range of nearly 100 nm. A single-lobe far-field mode was maintained over most of the driving current dynamic range, with a full width at half-maximum (FWHM) ranging from 10.6° to 13.2°. At 20°C, the peak output power of the device with a cavity length of 2 mm reaches 3.36 W.

2. DESIGN AND FABRICATION

According to the mid-infrared characteristic absorption of the target gases (N_2O, CH_4, and C_2H_6), we set the working wavelength around 7 μm in this work.

A bound-to-continuous state transition is introduced into the active region design, which is composed of a 50-stage strain compensated $In_{0.6}Ga_{0.4}As/In_{0.44}Al_{0.56}As$ material system. The specific layer thickness sequence of the active region in a single period from the injection barrier is given as follows: **1.8**/3.9/**1.0**/4.7/**0.9**/5.06/**0.9**/1.7/**4**/2.6/**2.8**/2.7/**1.9**/2.8/**1.7**/3.2 (nm), where the $In_{0.44}Al_{0.56}As$ barrier layers are shown in bold, the $In_{0.6}Ga_{0.4}As$ wells are normal, and the n-doped layers (Si, 1.5×10^{17} cm^{-3}) are underlined. The transition matrix elements from the upper level to the two lower levels in this material structure are 1.42 and 1.38 nm, respectively, and thus the transition to lower levels can be achieved. Moreover, multiple energy levels in the injection region form quasi-continuous injection into the upper level, preventing the energy levels from staggering sensitively with increasing voltage. Thus, the gain spectrum can be broadened effectively over a large voltage range. This ensures that the gain linewidth for multiple wavelengths remains within the large current tuning range to achieve simultaneous emission of multi-wavelengths.

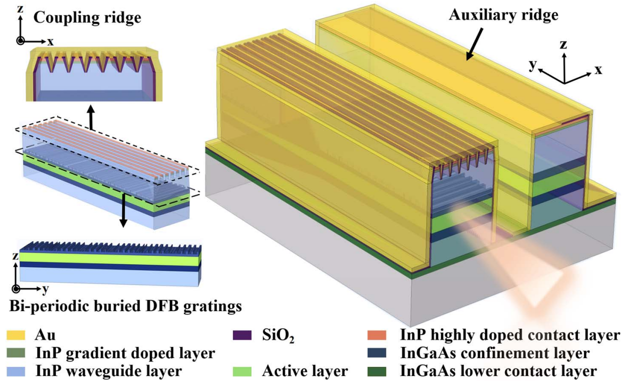

Fig. 1. Three-dimensional device structure diagram of coupled ridge dual-wavelength DFB QCL.

The active region and InGaAs confinement layers were grown by molecular beam epitaxy, and the InP cladding was regrown by metal-organic vapor phase epitaxy (MOVPE). Starting from the semi-insulating (SI) InP substrate, the epitaxial structure is shown in Fig. 1: the $In_{0.53}Ga_{0.47}As$ high doping lower contact layer (0.2 μm, Si, 3×10^{18} cm^{-3}), InP bottom waveguide layer (5 μm, Si, 3×10^{16} cm^{-3}), $In_{0.53}Ga_{0.47}As$ confinement layer (200 nm, Si, 4×10^{16} cm^{-3}), active region, $In_{0.53}Ga_{0.47}As$ confinement layer (300 nm, Si, 3×10^{16} cm^{-3}), InP upper waveguide layer (3 μm, Si, 3×10^{16} cm^{-3}), InP gradient-doped layer (150 nm, Si, 1×10^{17} to 5×10^{17} cm^{-3}), and InP highly doped contact layer (850 nm, Si, 5×10^{18} cm^{-3}) are grown sequentially.

A. Bi-Periodic Compound Gratings for Longitudinal Mode Control

Figure 2(a) shows the electroluminescence (EL) spectrum of the material, which contains two gain peaks with a significant overlap. To approach the maximum gain value and consider the waveguide loss difference caused by the free carrier absorption, λ_1 is selected near the gain center, and λ_2 is selected to be tens of wavenumbers blue-shifted relative to the higher gain peak position. These wavelengths satisfy the requirements for each mode to be close to the maximum value of its corresponding gain peak and ensure a sufficient gain bandwidth to achieve simultaneous lasing. In addition, the lasing peak should encompass the signals of multiple gases. After comprehensive consideration, the final wavelengths were defined as $\lambda_1 = 7.5$ μm and $\lambda_2 = 7.05$ μm.

The first-order grating periods are selected as $\Lambda_1 = 1.173$ μm and $\Lambda_2 = 1.093$ μm, which satisfy the Bragg condition for lasing at $\lambda_1 = 7.5$ μm and $\lambda_2 = 7.05$ μm, respectively. As demonstrated in Fig. 1, the buried gratings are prepared in the upper confinement layer. To realize dual-wavelength lasing, the coupling coefficients at the two wavelengths must be similar. From Fig. 2(b), similar coupling

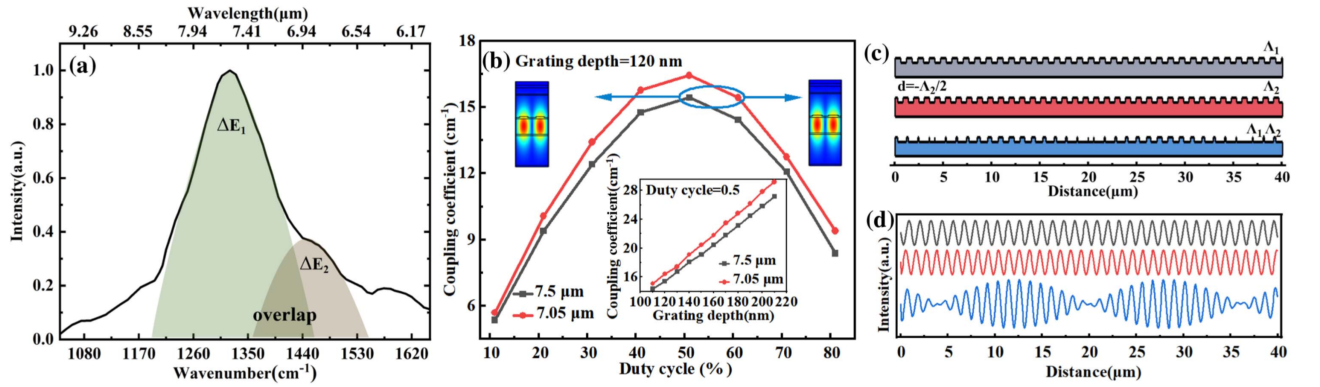

Fig. 2. (a) Electroluminescence spectrum of the materials. ΔE_1 and ΔE_2 represent the gain spectra from the upper energy level to the two lower energy levels, respectively. (b) Coupling coefficient varies with the grating duty cycle and grating depth for the two wavelengths. The upper insets show the calculated modal profiles of λ_1 emission with $\sigma = 0.5$ (left) and λ_2 emission with $\sigma = 0.6$ (right), respectively. (c) Schematic diagram of bi-period grating formed by different photolithographic stripes. (d) The propagation waves correspond to the gratings of the same color in Fig. 1(c).

coefficients are obtained when the grating depth is 120 nm, and the grating duty cycles σ values of λ_1 and λ_2 are 0.5 and 0.6, respectively.

Bi-periodic compound gratings nested within each other were fabricated by wet etching after two consecutive holographic exposures. The etching morphologies of the single-period and bi-periodic gratings are shown in Fig. 2(c). The longitudinal mode selection mechanisms of the superimposed double gratings are independent of each other. The corresponding propagation wave of grating 1 [shown as the gray curve in Fig. 2(d)] can be expressed as $f_1(x) = \sin(\frac{2\pi x}{\Lambda_1})$, where x is the distance from the cavity surface along the cavity length direction. The grating formed by the second holographic exposure [shown as the red curve of Fig. 2(d)] forms an uncertain initial phase $\alpha = \frac{2\pi d}{\Lambda_2}$ relative to grating 1 because of the spatial position offset d. The propagation wave corresponding to this grating can be simply expressed as $f_2(x) = \sin(\frac{2\pi x}{\Lambda_2} + \alpha)$. Finally, the propagating waves in the superimposed composite grating [shown in the blue pattern in Fig. 2(d)] can be expressed as $f(x) = f_1(x) + f_2(x)$. From the sum function operation of the trigonometric function, it is known that the period of $f(x)$ is the least common multiple of Λ_1 and Λ_2, independent of α. That is, the spatial position offset d of two gratings only affects the initial phase of the interference wave and does not affect the mode selection mechanism. This method can be extended to more wavelengths. And it is worth noting that higher etching accuracy is required when the number of wavelengths is increased.

B. Coherent Coupling Ridge Array for Optimizing Transverse Mode and High Output Power

The coherent coupling ridge can provide transverse mode control under the premise of high output power. The design of coherent ridge arrays is mainly related to three parameters: etching depth D, period of ridge P, and width of single ridge W_S. The coupling ridge structure is confined to the upper InP waveguide layer and does not reach the active region, so this etching depth D ensures that different ridge waveguides share only one active region. It avoids a low coupling coefficient being caused by the independence of the active regions of the coherent arrays and contributes to improved far-field beam quality. At the same time, it also avoids the problem of insufficient refractive index contrast between the etched and non-etched regions originating from small etching depth D. Moreover, to promote the formation of fundamental supermodes, it is necessary to concentrate the mode intensity under the ridge waveguide to enhance the coupling between adjacent ridges. Therefore, the ridge width W_S should be as large as possible under the determined ridge period P.

The mode selection mainly depends on the mode waveguide loss difference [29]. The corresponding waveguide absorption loss $\alpha(\omega)$ was then calculated after obtaining the complex refractive index $\tilde{n}$ for different modes. $\tilde{n}$ and $\alpha(\omega)$ can be expressed as

$$\tilde{n} = n(\omega) + i\kappa(\omega), \quad (1)$$

$$\alpha(\omega) = \kappa_0 \kappa(\omega), \quad \kappa_0 = \frac{2\pi}{\lambda_0}, \quad (2)$$

where κ_0 is the vacuum wave vector. The order of magnitude of κ_0 is 10^{-5}, and the loss is extremely sensitive to changes in $\kappa(\omega)$. Therefore, the loss difference value is only indicative, and the actual W_S is mainly determined by the practical lateral corrosion degree of wet corrosion. Here, the effects of ridge period and etching depth on supermode loss are simulated and discussed (taking λ_1 as an example, and a similar analysis was conducted on λ_2). The simulation results of λ_1 indicate that, although a smaller ridge period P is beneficial for obtaining an in-phase fundamental supermode, the waveguide loss is relatively high [Fig. 3(a)]. The excessively large period may only satisfy higher-order supermodes. Moreover, a low etching depth D may be insufficient to produce the fundamental supermode, and the excessive etching depth leads to a large loss [Fig. 3(b)]. Carrying out the same analysis on λ_2, the final ridge period and the etching depth should be kept within 9–11 and 2.3–2.45 μm, respectively, to ensure a large mode loss difference and a low fundamental supermode loss. The fundamental supermode near-field profiles of the seven-element coupled ridge waveguide structure at 7.05 and 7.5 μm are shown in Figs. 3(c) and 3(d), respectively. The field strength

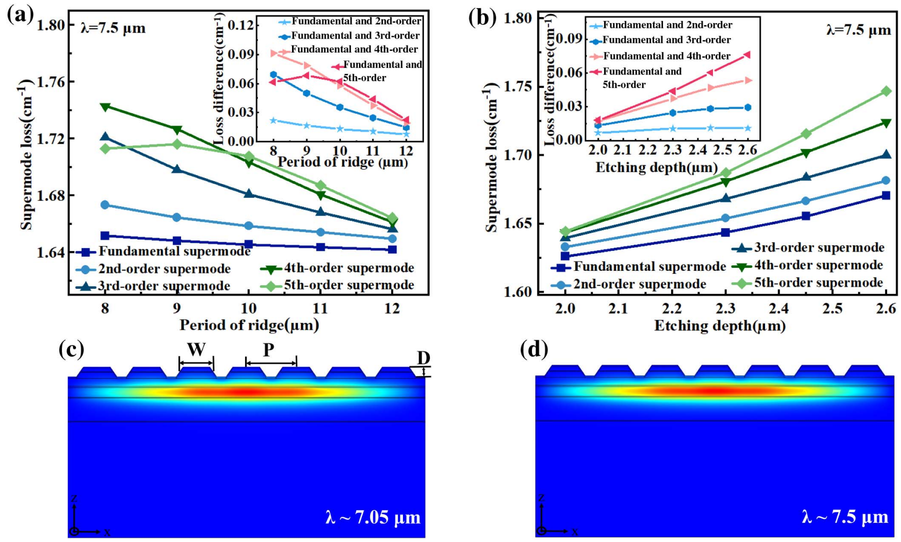

Fig. 3. Dependences of supermode loss and loss difference on (a) ridge period and (b) array etching depth at $\lambda_1 = 7.5$ μm. Fundamental supermode near-field profiles of the seven-element coupled ridge waveguide structure at (c) $\lambda_1 = 7.05$ μm and (d) $\lambda_1 = 7.5$ μm calculated using COMSOL finite element method software.

is concentrated in the center of the active area, indicating the in-phase operation in each ridge element.

In the practical chip process, the upper waveguide layer of InP was removed down to the first InGaAs layer, using concentrated HCl as a selective wet etch solution. First-order Bragg gratings for Λ_1 were exposed by optical lithography, then the turning platform of the holographic exposure system was shifted to the angle corresponding to Λ_2, and the exposure time was decreased to prepare the grating 2 with $\sigma_2 = 0.6$. After using a photomask where the grating patterns had been defined on the InGaAs confinement layer by wet etching, then the upper InP layers were regrown over the gratings using MOVPE. After secondary epitaxy, coupling ridge arrays were prepared by lithography and wet chemical etching. Parameters chosen for the actual coupling ridge structures 1 and 2 are shown in Fig. 4(a). As an SI InP substrate is used in this device, the coplanar electrode design is adopted. To improve the heat dissipation capability of the device, the laser is mounted epi-side down on an AlN submount. In this way, the auxiliary ridge must cooperate with the graphite heat sink, as shown in Fig. 4(b), to achieve the purpose of leading wires from the electrode. So, we alternately etched and smoothed the corrosion interface until the lower contact layer of InGaAs was exposed to form an auxiliary ridge acting as an electrode on the same surface. Subsequently, an insulation layer of SiO_2 film was deposited, which left an electric injection window formed by dry etching, and electrical contact was provided by a Ti/Au layer deposited through electron beam evaporation. An additional 5-μm-thick gold layer was electroplated to further improve the heat dissipation. After being thinned down, the final device structure is shown in Fig. 1. We combined the coupled ridges along the ridge width direction x for transverse mode control and the bi-period composite gratings along the cavity length direction y for longitudinal mode selection. The two are, respectively, located on the upper confinement layer and the upper waveguide layer in the material growth direction z.

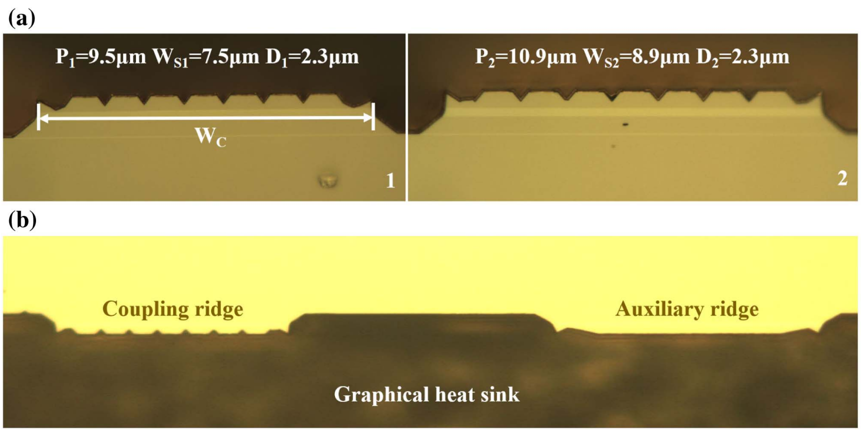

Fig. 4. (a) Cross-sectional photographs of the actual coupling ridge portions for parameter sets 1 (left) and 2 (right). (b) Cross-sectional photograph of actual device mounted epi-side down onto the graphite heat-sink.

3. RESULTS AND DISCUSSION

The device was characterized using a thermoelectric cooler. The spectra were measured by Fourier transform infrared spectroscopy in rapid scanning mode, with a resolution of 0.25 cm^{-1}. The emitted optical power was measured using a calibrated thermopile detector placed in front of the laser.

We present the light power-current-voltage (L-I-V) characteristics of a seven-element coupled ridge array with a cavity length of 2 mm, ridge period (P_1) of 9.5 μm, and single ridge width (W_{S1}) of 7.5 μm (total coupled ridge width $W_{C1} = 75$ μm) at a driving repetition rate of 10 kHz and a pulse width of 1 μs. Typical L-I-V characteristics at different heat-sink temperatures ranging from 10°C to 40°C are shown in Fig. 5(a). At 20°C, the threshold currents are 1.4 A (I_{th1}) for λ_1 (7.5 μm) and 2.2 A (I_{th2}) for λ_2 (7.01 μm). A peak output power up to 3.36 W was obtained under dual-mode operation with a slope efficiency of 0.798 W/A and a wall plug efficiency of 3.11%. To prevent damage, the maximum operating current was not evaluated.

Apart from devices of size 1, we also prepared another seven-element coherent ridge array 2 for comparison, with a total coupled ridge width W_{C2} of 90 μm. It is generally accepted that the device output power increases with increasing ridge width, and the supermode loss of size 1 at the two wavelengths is smaller than that of size 2 in the theoretical simulations. However, the measured peak output power does not increase significantly, as shown in Fig. 5(b). Simultaneously, the device threshold becomes higher. Moreover, even for size 1 devices with longer cavity lengths of 3 mm, the power does not increase with an increasing cavity length. Based on the phenomena discussed above, we consider that the heat accumulation in the active regions is greater than that of size 1 with 2 mm cavity length, which is unfavorable for output power enhancement. In addition, the waveguide loss caused by side wall roughness in the coupled ridge array is a potential reason for the increased device threshold and limited output power. Therefore, the coherent coupled ridge structure cannot reach high powers by simply increasing the active region volume, even if it meets the requirements for the fundamental supermode in the simulations.

The far-field patterns of the laser arrays in the ridge width direction are of the most concern. The diffraction limit angles calculated for a 75-μm-wide aperture array are $DL_1 = 7.007°$ and $DL_2 = 6.548°$ at $\lambda_1 = 7.5$ μm and $\lambda_2 = 7.01$ μm, respectively. The far-field distribution along the ridge width direction under the influence of the coherence between the interval emission regions was measured at a driving repetition frequency of 3 kHz and a pulse width of 1 μs. As shown in Fig. 6(a), single-wavelength lasing was measured before the dual-mode operation was triggered, and the devices showed single-lobe far-field distributions along the ridge width direction. The FWHM of the far-field pattern is 4.9° when $I = 1.6$ A, and the FWHM is close to DL_1. Figure 6(b) shows the far-field distribution under the dual-mode operation at room temperature. The FWHMs of the far-field pattern range from 10.6° to 13.2°, corresponding to $1.51 \times DL_1$ and $1.88 \times DL_1$ for the dominant wavelength at the time, respectively. These results indicate that the operations are in phase in each ridge unit at different currents.

It should be noted that, as the driving current continues to increase (e.g., for $I > 3$ A), the high-order supermode acquires sufficient gain, and side lobes gradually appear symmetrically outside the center, which primarily appeared at angles of $\pm(11°–13°)$ and $\pm(22°–24°)$. According to Fraunhofer's multiple slit diffraction model, the total far-field intensities of the phase-locked array represent the joint effects of single-emitter diffraction and interference from periodically spaced emitters [30]. The interference distribution of the bright stripes is determined by the following equation:

$$P \sin(\theta) = \pm\left[k + \frac{\delta}{2\pi}\right]\lambda, \tag{3}$$

where P is the ridge period, θ is the diffraction angle, and δ is the phase shift between adjacent ridges. In our example, P is 9.5 μm ($k = 0$), and when $\delta = 0, \pi/2$, and π, the calculated θ values for $\lambda_1 = 7.5$ μm are 0°, ±11.38°, and ±23.25°, and the θ values for $\lambda_2 = 7.01$ μm are 0°, ±10.63°, and ±21.65°, respectively. These calculated values are consistent with the experimental results. Based on the discussion above, we consider the high-order supermode with the $\pi/2$ phase shift

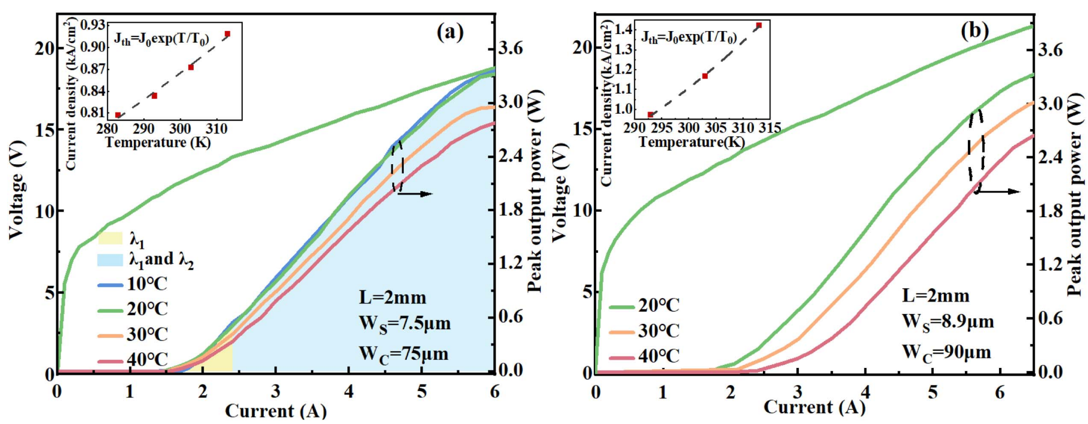

Fig. 5. (a) L-I-V curves at T_{sink} from 10°C to 40°C for a 2-mm-long QCL with ridge width $W_{S1} = 7.5$ μm. The inset shows J_{th} as a function of T in pulsed mode. The dashed line is the fitting result obtained using the exponential function $J_{th} = J_0 \exp(T/T_0)$. (b) L-I-V curves at T_{sink} from 20°C to 40°C for a 2-mm-long QCL with ridge width $W_{S2} = 8.9$ μm.

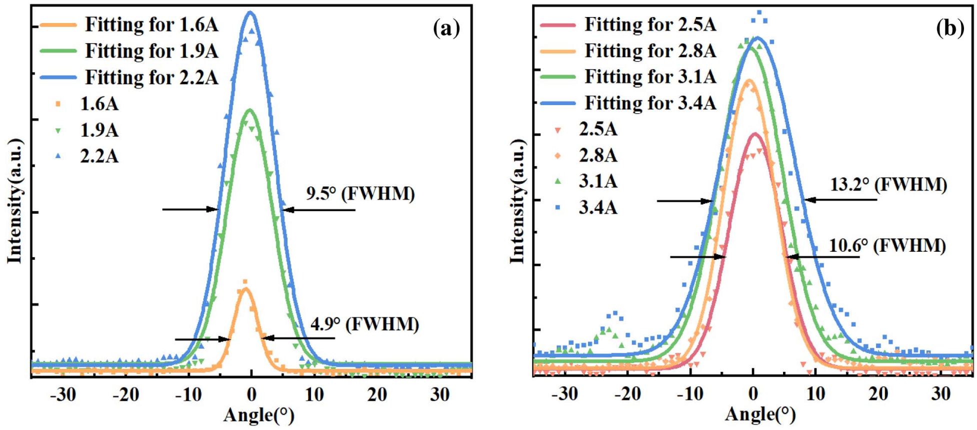

Fig. 6. Far-field profile along the ridge width direction at room temperature for a device with ridge period $P_1 = 9.5$ μm, ridge width $W_{S1} = 7.5$ μm, and depth $D_1 = 2.3$ μm. (a) Before λ_2 lasing. (b) Lasing at dual wavelengths. Data fittings performed using the Gaussian function are represented by solid lines.

to be the cause of the FWHM increase in the far-field center lobe. The FWHM of the side lobe at ±23.53° is 7.14°, which is similar to 7.007° for DL_1. This indicates that the high-order supermode with the π phase shift contributes to the appearance of these side lobes. These results demonstrate that a large ridge width inevitably causes the higher-order mode to be excited at high currents, and the difference in loss between the fundamental supermode and the higher-order mode is insufficient to provide a pure fundamental supermode. However, the power is still obviously concentrated within the center lobe, which remains high for applications that require high power but do not have strict far-field requirements.

To characterize the lasing characteristics of the dual-mode QCL more clearly, we first tested the driving current tuning spectra of the device above the threshold at 20°C, with results shown in Fig. 7(a). When the injection current ranges from 1.4 to 2.2 A, the laser presents only λ_1 single-mode lasing, and when the injection current exceeds 2.2 A and is within a large dynamic range, the dual wavelengths of the QCL can be simultaneously lasing. In addition, because the device threshold current increases with increasing temperature, we measured the temperature-tunable spectra under the condition that single-mode lasing was ensured at the two wavelengths. As shown in Fig. 7(b), the change in lasing wavelength λ_1 with temperatures from 1333.415 cm^{-1} at −4°C to 1325.58 cm^{-1} at 60°C was obtained with a temperature tuning coefficient of −0.116 cm^{-1} K^{-1}. For λ_2, the wavelength changed from 1428.151 to 1419.723 cm^{-1} with a tuning coefficient of −0.121 cm^{-1} K^{-1} within the same temperature range. As indicated in the insets of Fig. 7(c), an SMSR exceeding 20 dB was achieved for λ_1 and λ_2. In addition, during temperature tuning, both wavelengths maintained stable tuning without any mode hopping.

Increases in temperature and current cause the lasing wavelength to be red-shifted linearly; therefore, a combination of current tuning and temperature tuning can broaden the tuning range. As depicted in the upper part of Fig. 7(c), the spectra can cover 1324.616 cm^{-1} (60°C, 4 A) to 1333.415 cm^{-1} (−4°C, 1.5 A) and 1418.425 cm^{-1} (60°C, 4 A) to 1428.151 cm^{-1} (−4°C, 2.3 A). The total tuning range reaches approximately 100 nm.

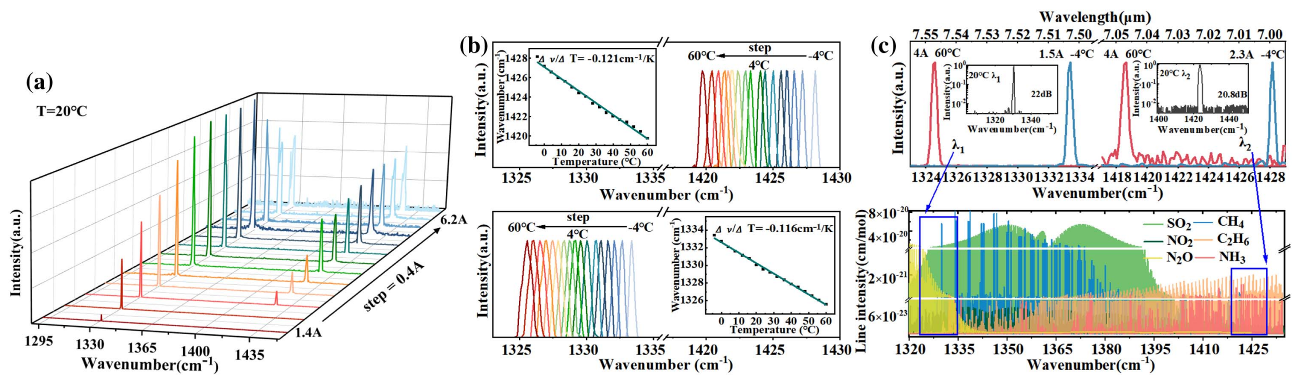

Fig. 7. (a) Optical spectra measured by varying the current at room temperature (20°C). (b) Emission spectra of the device during operation when T was varied from −4°C to 60°C in increments of 4°C (measured at 1.05 × I_{th}). The insets show the linearly fitted tuning characteristics of lasing frequency versus injection temperature. (c) The upper part, spectrum of the tuning range combined with temperature and current tuning. The insets are single-mode spectra of the λ_1 and λ_2 emissions at 20°C with SMSR of over 20 dB. The lower part, the absorption lines of gas molecules within the tuning range.

The temperature and current conditions corresponding to each wavelength can be determined via measurements. In the lower part of Fig. 7(c), the laser covers the spectrum for the molecular absorption lines of multiple gases, such as N_2O and C_2H_6, whose molecular absorption lines do not overlap [11]. It can also be used for the simultaneous detection of C_2H_6 and CH_4 to improve methane leakage detection [31].

4. CONCLUSION

In conclusion, using superimposed buried bi-periodic DFB gratings and a coupled ridge array, we demonstrate a stacked 3D monolithic integrated dual-mode QCL with high peak output power. A seven-element QCL array was simulated and fabricated to explore the coherence of the coupled ridge waveguide structures. It was observed that the far-field distribution of the main lobe remained stable in the ridge width direction during dual-wavelength lasing. The peak output power reached up to 3.36 W at 20°C. With current or temperature tuning processes, the device maintained mutually independent double longitudinal modes without mode hopping, and the temperature tuning coefficients were −0.116 and −0.121 $cm^{-1}\,K^{-1}$ at λ_1 and λ_2, respectively. By combining the current and temperature tuning modes, the whole spectrum can cover nearly 100 nm. The wide optical coverage, high output power, and beneficial single-lobe far-field distribution of this QCL are advantageous for practical application in high-resolution multi-gas detection (N_2O, C_2H_6, CH_4, etc.) and medical analysis. Further research can be combined with the AWG structure on the InGaAs/InP material platform. By pumping the single laser, a multi-wavelength high-power integrated laser source with high beam quality is obtained to detect more gases.

Funding. National Key Research and Development Program of China (2021YFB3201901); National Natural Science Foundation of China (61835011, 61991430, 62335015); Key Program of the Chinese Academy of Sciences (XDB43000000).

Acknowledgment. The authors thank Ping Liang for her help in device processing.

Disclosures. The authors declare no conflicts of interest.

Data Availability. The data that support the findings of this study are available from the corresponding author upon reasonable request.

REFERENCES

1. J. Faist, F. Capasso, D. Sivco, C. Sirtori, A. Hutchinson, and A. Cho, "Quantum cascade laser," Science **264**, 553–556 (1994).
2. S. Blaser, D. A. Yarekha, L. Hvozdara, Y. Bonetti, A. Muller, M. Giovannini, and J. Faist, "Room-temperature, continuous-wave, single-mode quantum-cascade lasers at $\lambda \approx 5.4$ μm," Appl. Phys. Lett. **86**, 041109 (2005).
3. Y. Bai, S. Tsao, N. Bandyopadhyay, S. Slivken, Q. Y. Lu, D. Caffey, M. Pushkarsky, T. Day, and M. Razeghi, "High power, continuous wave, quantum cascade ring laser," Appl. Phys. Lett. **99**, 261104 (2011).
4. Y. G. Guan, X. Y. Lu, F. M. Cheng, J. Q. Liu, L. J. Wang, N. Zhuo, J. C. Zhang, S. Q. Zhai, S. M. Liu, and F. Q. Liu, "Continuous-wave distributed Bragg reflector quantum cascade lasers with fine single-mode tuning up to 102°C at $\lambda \sim 8.4$ μm," Opt. Commun. **528**, 128994 (2023).
5. S. M. Miller, S. C. Wofsy, A. M. Michalak, E. A. Kort, A. E. Andrews, S. C. Biraud, E. J. Dlugokencky, J. Eluszkiewicz, M. L. Fischer, G. Janssens-Maenhout, B. R. Miller, J. B. Miller, S. A. Montzka, T. Nehrkorn, and C. Sweeney, "Anthropogenic emissions of methane in the United States," Proc. Natl. Acad. Sci. USA **110**, 20018–20022 (2013).
6. K. D. Skeldon, L. C. McMillan, C. A. Wyse, S. D. Monk, G. Gibson, C. Patterson, T. France, C. Longbottom, and M. J. Padgett, "Application of laser spectroscopy for measurement of exhaled ethane in patients with lung cancer," Respir. Med. **100**, 300–306 (2006).
7. G. W. Santoni, B. C. Daube, E. A. Kort, R. Jiménez, S. Park, J. V. Pittman, E. Gottlieb, B. Xiang, M. S. Zahniser, D. D. Nelson, J. B. McManus, J. Peischl, T. B. Ryerson, J. S. Holloway, A. E. Andrews, C. Sweeney, B. Hall, E. J. Hintsa, F. L. Moore, J. W. Elkins, D. F. Hurst, B. B. Stephens, J. Bent, and S. C. Wofsy, "Evaluation of the airborne quantum cascade laser spectrometer (QCLS) measurements of the carbon and greenhouse gas suite–CO_2, CH_4, N_2O, and CO–during the CalNex and HIPPO campaigns," Atmos. Meas. Tech. **7**, 1509–1526 (2014).
8. J. Sinclair, P. G. J. Irwin, E. Wilson, and S. Calcutt, "Detectability of trace gases in the Martian atmosphere using gas correlation filter radiometry," in *European Planetary Science Congress* (2015), paper EPSC2015-376.
9. T. I. Yacovitch, S. C. Herndon, J. R. Roscioli, C. Floerchinger, R. M. McGovern, M. Agnese, G. Pétron, J. Kofler, C. Sweeney, A. Karion, S. A. Conley, E. A. Kort, L. Nähle, M. Fischer, L. Hildebrandt, J. Koeth, J. B. McManus, D. D. Nelson, M. S. Zahniser, and C. E. Kolb, "Demonstration of an ethane spectrometer for methane source identification," Environ. Sci. Technol. **48**, 8028–8034 (2014).
10. X. Tian, Y. Cao, J. J. Chen, K. Liu, G. S. Wang, T. Tan, J. X. Mei, W. D. Chen, and X. M. Gao, "Dual-gas sensor of CH_4/C_2H_6 based on wavelength modulation spectroscopy coupled to a home-made compact dense-pattern multipass cell," Sensors **19**, 820 (2019).
11. J. Kostinek, A. Roiger, K. J. Davis, C. Sweeney, J. P. DiGangi, Y. Choi, B. Baier, F. Hase, J. Groß, M. Eckl, T. Klausner, and A. Butz, "Adaptation and performance assessment of a quantum and interband cascade laser spectrometer for simultaneous airborne *in situ* observation of CH_4, C_2H_6, CO_2, CO and N_2O," Atmos. Meas. Tech. **12**, 1767–1783 (2019).
12. N. W. Liu, L. G. Xu, S. Zhou, L. Zhang, and S. J. Li, "Simultaneous detection of multiple atmospheric components using an NIR and MIR laser hybrid gas sensing system," ACS Sens. **5**, 3607–3616 (2020).
13. B. G. Lee, H. A. Zhang, C. Pflügl, L. Diehl, M. A. Belkin, M. Fischer, A. Wittmann, J. Faist, and F. Capass, "Broadband distributed-feedback quantum cascade laser array operating from 8.0 to 9.8 μm," IEEE Photonics Technol. Lett. **21**, 914–916 (2009).
14. T. S. Karnik, K. P. Dao, Q. Du, L. Diehl, C. Pflügl, D. Vakhshoori, and J. Hu, "High-efficiency mid-infrared InGaAs/InP arrayed waveguide gratings," Opt. Express **31**, 5056–5068 (2023).
15. J. S. Yu, S. Slivken, S. R. Darvish, A. Evans, B. Gokden, and M. Razeghi, "High-power, room-temperature, and continuous-wave operation of distributed-feedback quantum-cascade lasers at $\lambda \sim 4.8$ μm," Appl. Phys. Lett. **87**, 041104 (2005).
16. Q. Y. Lu, Y. Bai, N. Bandyopadhyay, S. Slivken, and M. Razeghi, "Room-temperature continuous wave operation of distributed feedback quantum cascade lasers with watt-level power output," Appl. Phys. Lett. **97**, 231119 (2010).
17. Y. J. Guan, L. J. Wang, N. Zhuo, J. C. Zhang, S. Q. Zhai, J. Q. Liu, S. M. Liu, and F. Q. Liu, "Dual-wavelength switchable, mid-infrared quantum cascade laser with two shallow-etched distributed Bragg reflectors," Opt. Express **29**, 39376–39383 (2021).
18. F. Kapsalidis, M. Shahmohammadi, M. J. Süess, J. M. Wolf, E. Gini, M. Beck, M. Hundt, B. Tuzson, L. Emmenegger, and J. Faist, "Dual-wavelength DFB quantum cascade lasers: sources for multi-species trace gas spectroscopy," Appl. Phys. B **124**, 107 (2018).
19. Q. Y. Lu, S. Slivken, N. Bandyopadhyay, Y. Bai, and M. Razeghi, "Widely tunable room temperature semiconductor terahertz source," Appl. Phys. Lett. **105**, 201102 (2014).

20. Q. Y. Lu, N. Bandyopadhyay, S. Slivken, Y. Bai, and M. Razeghi, "Room temperature single-mode terahertz sources based on intracavity difference-frequency generation in quantum cascade lasers," Appl. Phys. Lett. **99**, 131106 (2011).
21. S. R. Darvish, W. Zhang, A. Evans, J. S. Yu, S. Slivken, and M. Razeghi, "High-power, continuous-wave operation of distributed-feedback quantum-cascade lasers at $\lambda \sim 7.8$ μm," Appl. Phys. Lett. **89**, 251119 (2006).
22. H. Kogelnik and C. V. Shank, "Coupled-wave theory of distributed feedback lasers," J. Appl. Phys. **43**, 2327–2335 (1972).
23. Y. F. Ma, R. Lewicki, M. Razeghi, and F. K. Tittel, "QEPAS based ppb-level detection of CO and N_2O using a high power CW DFB-QCL," Opt. Express **21**, 1008–1019 (2013).
24. M. Troccoli, "High-power emission and single-mode operation of quantum cascade lasers for industrial applications," IEEE J. Sel. Top. Quantum Electron. **21**, 61–67 (2015).
25. N. Yu, L. Diehl, E. Cubukcu, D. Bour, S. Corzine, G. Hofler, A. K. Wojcik, K. B. Crozier, A. Belyanin, and F. Capasso, "Coherent coupling of multiple transverse modes in quantum cascade lasers," Phys. Rev. Lett. **102**, 013901 (2009).
26. L. J. Mawst and D. Botez, "High-power mid-infrared ($\lambda \sim 3$–6 μm) quantum cascade lasers," IEEE Photonics J. **14**, 1508025 (2022).
27. S. D. Cin, F. Pilat, A. Konečný, N. Opačak, G. Strasser, and B. Schwarz, "Coherent control of transverse modes in semiconductor laser frequency combs via radio-frequency injection," Appl. Phys. Lett. **121**, 071106 (2022).
28. D. Botez, "Array-mode far-field patterns for phase-locked diode-laser array: coupled-mode theory versus simple diffraction theory," IEEE J. Quantum Electron. **21**, 1752–1755 (1985).
29. Y. H. Liu, J. C. Zhang, F. L. Yan, F. Q. Liu, N. Zhuo, L. J. Wang, J. Q. Liu, and Z. G. Wang, "Coupled ridge waveguide distributed feedback quantum cascade laser arrays," Appl. Phys. Lett. **106**, 142104 (2015).
30. F. L. Yan, J. C. Zhang, Z. W. Jia, N. Zhuo, S. Q. Zhai, S. M. Liu, F. Q. Liu, and Z. G. Wang, "High-power phase-locked quantμm cascade laser array emitting at $\lambda \sim 4.6$ μm," AIP Adv. **6**, 035022 (2016).
31. W. L. Ye, C. G. Li, C. T. Zheng, N. P. Sanchez, A. K. Gluszek, A. J. Hudzikowski, L. Dong, R. J. Griffin, and F. K. Tittel, "Mid-infrared dual-gas sensor for simultaneous detection of methane and ethane using a single continuous-wave interband cascade laser," Opt. Express **24**, 16973–16985 (2016).